Contemporary Mathematics
https://ojs.wiserpub.com/index.php/CM/

Research Article

Transient Modeling for Faster Gas Sensor Response: An Efficient Mathematical Approach for MOX Sensors in Ethanol Detection

Ata Jahangir Moshayedi[1], Mohammad Hadi Noori Skandari[2], Jiandong Hu[3], Abolfazl Razi[4], David Bassir[5,6*]

[1] School of Information Engineering, Jiangxi University of Science and Technology, No 86, Hongqi Ave, Ganzhou, 341000, Jiangxi, China
[2] Faculty of Mathematical Sciences, Shahrood University of Technology, Shahrood, Iran
[3] Key Laboratory of Wheat and Maize Crop Science, Henan Agricultural University, Zhengzhou, 450002, Henan, China
[4] School of Computing, Clemson University, Clemson, SC, 29634, USA
[5] Smart Structural Health Monitoring and Control Laboratory, DGUT-CNAM, Dongguan University of Technology, D1, Daxue Rd., Songshan Lake, Dongguan, 523000, Guangdong, China
[6] ENS-Paris-Saclay University, Centre Borelli, UMR CNRS 9010, Gif-sur-Yvette, 91190, France
E-mail: david.bassir@ens-paris-saclay.fr

Received: 28 May 2025; **Revised:** 6 October 2025; **Accepted:** 17 October 2025

Abstract: Gas sensor modeling remains a persistent challenge in sensor research, playing a vital role in enhancing performance, calibrating outputs, and developing robust detection algorithms. Among various sensor types, metal oxide gas sensors, often embedded in electronic nose systems, face significant issues such as sensitivity to humidity and temperature fluctuations, complex calibration needs, cross-sensitivity to other gases, and slow response times. Addressing these limitations is crucial for improving sensor accuracy and reliability. This paper introduces a novel modeling approach for the behavior of the metal oxide gas sensor TGS 2620 in the transient domain, with a focus on capturing the effects of temperature and humidity. The proposed model is based on the Gaussian function, chosen for its mathematical simplicity, smoothness, statistical relevance, and broad applicability. By applying this function within a new framework, we aim to improve calibration accuracy and enhance the interpretation of sensor responses under dynamic conditions. Experimental data were obtained through rigorous laboratory testing, using an ENose system equipped with TGS 2620 sensors exposed to varying temperature and humidity levels. The dataset includes 800 samples across gas concentrations ranging from 60 to 400 ppm. Complementary numerical simulations were performed to further analyze sensor dynamics. Our results demonstrate the effectiveness of modeling the sensor's transient response, enabling more accurate estimation of gas concentrations under fluctuating environmental conditions. This work has broader implications in environmental monitoring, industrial safety, and healthcare by enhancing sensor performance for early detection of hazardous gases, ultimately contributing to public safety and quality of life.

Keywords: transient time, gas sensor response, gas sensors, Electronic Nose (ENose), metal oxide gas sensor, mathematical modeling

MSC: 93B30, 41A30, 65D15

Copyright ©2026 David Bassir, et al.
DOI: https://doi.org/10.37256/cm.7120267320
This is an open-access article distributed under a CC BY license
(Creative Commons Attribution 4.0 International License)
https://creativecommons.org/licenses/by/4.0/

1. Introduction

Gas sensors detect and measure specific gases using mechanisms such as chemical reactions, infrared absorption, or conductivity changes, and are widely applied in environmental monitoring, industrial safety, and leak detection [1]. Different types exist-electrochemical (e.g., Carbon Monoxide, Hydrogen$_2$S), catalytic (combustible gases), semiconductor, piezoelectric, Surface Acoustic Wave (SAW), optical, thermal conductivity, and solid-state sensors-chosen based on specificity, sensitivity, and application needs [2, 3]. Among these, Metal Oxide (MOX) sensors are favored for their high sensitivity, fast response, cost-effectiveness, compact size, and low power consumption, making them suitable for consumer electronics, industrial monitoring, and safety systems [1, 2]. In gas sensor research, modeling is essential for improving performance, optimizing deployment, reducing costs, and ensuring accuracy across applications [4, 5]. Studies show that modeling enhances efficiency by incorporating environmental factors, leading to better understanding of sensor behavior and enabling new applications [6, 7]. It also supports calibration, ensuring precision, reliability, and consistency in measurements [8] (see Figure 1).

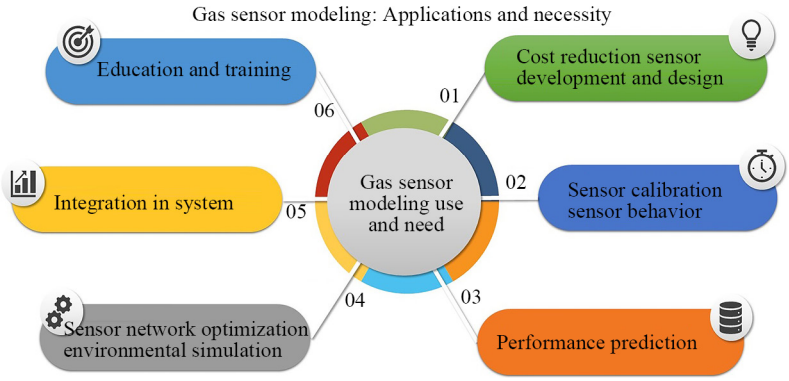

Figure 1. Applications and research areas of gas sensor modeling

Gas sensor modeling supports diverse domains including innovation, calibration, environmental monitoring, safety, industrial processes, machine learning, and sensor networks, while also serving as an educational tool for students and professionals [9]. MOX sensors, however, exhibit nonlinear and time-varying behavior, leading to sudden changes in measurements due to dynamic gas variations or sensor faults. Several studies have developed mathematical models to simulate this behavior and optimize performance for transient gas detection [10].

Electronic Nose (ENose) systems play a crucial role in modeling by providing rich datasets for pattern recognition and prediction of sensor responses [1]. ENose is also applied in food quality control [11–13], medical diagnosis, environmental monitoring, industrial safety, and forensic analysis [10, 14–17], making it a cost-effective approach for accurate and reliable gas sensor modeling [18].

This research introduces a novel gas sensor model for ethanol odor, tailored for MOX sensors. The model employs Gaussian functions, selected for their effectiveness in capturing key sensor characteristics such as rise time, steady state, and decay time. Its parameters are described in detail, and validation against real sensor responses demonstrates its robustness and reliability for sensor modeling and analysis [19].

The objective is to achieve the following:

1. Showcasing and validating the effectiveness of utilizing the Transient Response Area of gas sensors for modeling and estimating gas concentrations, as opposed to the traditional approach based on the entire sensor area response.

2. Utilizing a new space of functions based on Gaussian functions to approximate the sensor response in transient time zone based on real acquired sensor data with a higher accuracy compared with other approximate methods.

3. Demonstrating that this space of functions possesses the universal approximation property, i.e. allowing for the approximation of any continuous functions with arbitrary accuracy.

4. Employing this space of functions for the first time to approximate sensor responses in gas systems.

5. Showing that a combination of functions in this space can approximate the sensor response behavior at different time intervals post-injection of gas. These behaviors (see Figure 2) typically include:

A) An increasing curve within a specific time interval $[0, t_1]$.

B) A decreasing curve in a short time span $[t_1, t_2]$.

C) A stable treatment over a certain time period $[t_2, t_3]$.

D) Curve goes to zero for $t \geq t_3$.

This property of gas systems can be approximated with a good accuracy by a linear combination of functions in suggested space.

6. We propose a model that is capable of approximating sensor responses in gas systems for any combination of temperature, humidity, and injected gas concentration (ppm).

Based on the obtained results and real acquired data, the authors believe this paper presents an innovative MOX sensor model for rapid analysis of temperature, humidity, and gas density effects on ethanol detection. Fast alcohol gas detection is crucial for safety, health, regulatory compliance, process control, product quality, and road safety.

The paper is structured as follows: Section 2 covers the problem statement and the previous model. Section 3 details the methodology, including the sampling method, sampling protocol, and sample size calculation. Section 4 presents the proposed mathematical model. Model verification and result discussion are addressed in Section 5. Finally, Section 6 contains the conclusion.

2. Problem statement and research background

In order to precise gas sensor response modeling, it's crucial to evaluate both the performance of sensor areas and the current mathematical models, as they outlined in the following.

2.1 *Gas sensor response area*

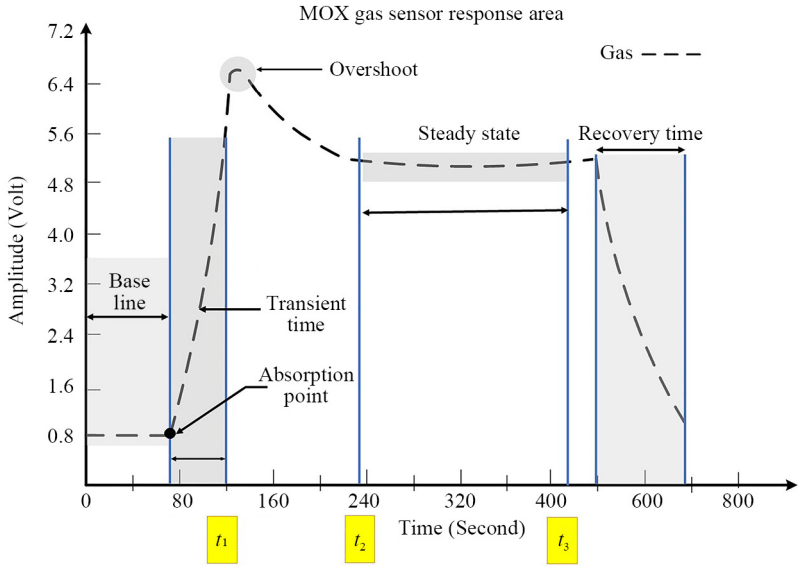

Figure 2. The Mox gas sensor response areas consist of baseline ($[0, t_1]$), adsorption, transient stage ($[t_1, t_2]$), overshoot, steady state ($[t_2, t_3]$), and recovery ($t \geq t_3$)

The response of a Mox gas sensor can often be divided into various parts or stages, each with distinct characteristics. These divisions help in understanding and modeling the sensor's behavior more comprehensively. Understanding the gas sensor's operation, especially the Mox gas sensor, involves examining its response across three crucial phases: transient time, steady state, and recovery time. Characterizing these phases is pivotal for assessing sensor performance, establishing response patterns, and ensuring precise gas detection across diverse applications, as depicted in Figure 2 [7, 20].

The gas sensor areas outlined, as depicted in Figure 2, are as follows:

1. Baseline: The baseline is the initial resistance or electrical output of the sensor in the absence of any target gas. It represents the sensor's equilibrium state when exposed to clean air or a reference gas.

2. Adsorption: When the sensor is exposed to a target gas, gas molecules adsorb onto the surface of the Mox material. This is the starting point for assessing changes in sensor response. This adsorption process is influenced by factors such as gas concentration, temperature, and the sensor's material properties.

3. Transitional Stage: The transitional stage represents the time it takes for the sensor's resistance or output to change from the baseline to a new, stable value in response to the presence of the target gas. This stage can vary in duration depending on the sensor's sensitivity and the gas concentration. Transient time signifies the initial phase of a sensor's reaction upon exposure to a gas. It denotes the duration needed for the sensor's signal to stabilize from its initial state to a consistent level. Within this phase, the sensor's output experiences fluctuations until it achieves a relatively stable condition, often characterized by the sensor response passing through an initial overshoot [21].

4. Steady-State Response: Once the sensor reaches a stable response level, it is said to be in the steady-state response. At this stage, the sensor's electrical properties (e.g., resistance) have stabilized, and the sensor is providing a consistent output signal corresponding to the gas concentration. Steady State as the stage after transient and overshoot shows, the sensor's output remains relatively constant and consistent, reflecting a stable and reliable reading of the gas concentration. This phase provides the baseline for accurate and continuous gas measurement, and the final stage is recovery time, which occurs when the sensor needs time to return to its initial state or baseline [22].

5. Recovery: When the sensor is removed from the target gas or exposed to clean air, it goes through a recovery stage. During this stage, the sensor's response gradually returns to the baseline. The recovery time can vary depending on factors like sensor design and gas concentration. In this area, indicating how quickly the sensor recovers to its initial state after being exposed to the gas. Between the mentioned areas, the transient time is crucial; it's important to strike a balance between achieving a rapid response and maintaining sensor stability and accuracy [23]. Dividing the sensor response into these parts or stages allows researchers and engineers to develop mathematical models and algorithms that describe each aspect of the sensor's behavior. It also helps in sensor calibration, signal processing, and improving the accuracy and reliability of gas concentration measurements in various applications [7].

2.2 *Mathematical gas sensor modeling*

The mathematical equations used to model the behavior of Mox gas sensors can vary depending on the specific sensor design, the target gas, and the desired level of accuracy. The reviewed model indicates that various mathematical equation models have been attempted to demonstrate the Mox gas sensor response behavior. The common proposed model. Each equation type serves a specific purpose in modeling gas sensor behavior, ranging from simple exponential decay to complex neural network and differential equation models. Table 1 [7] summarizes the deep review of the previously proposed mathematical model for describing the gas sensor behavior.

As shown in Table 1, the mathematical model consists of the following equations [26]:

• **Exponential Decay Model (Equation 1):** This model commonly used to describe the response of gas sensors over time. It includes key parameters: δ_1 represents the pre-temperature-change conductivity coefficient, δ_f signifies the conductivity coefficient at steady state under new heating conditions, δ_p is a modulator for temperature alterations, while τ symbolizes time, and τ denotes a crucial time constant integral to the sensor's dynamic behavior [27].

• **Arrhenius Equation (Equation 2):** This equation is used to model the temperature-dependent behavior of gas sensors. The variables R_{gas} and R_{air} respectively denote the sensor resistance in the presence of gas and air, while T_{gas} and T_{air} represent the sensor's temperature under gas and air environments. The constant B, intrinsic to the sensor's material and the specific target gas being analyzed, plays a pivotal role in this model [11–13]. This mathematical framework

forecasts the sensor's response by leveraging the fluctuations in electrical conductivity that transpire when the target gas interacts with the Mox material, as detailed in references [27–29].

• **Gas Concentration Model (Equation 3):** This equation models the relationship between the sensor resistance ratio (R/R_o). The parameter R represents the sensor resistance, while R_o signifies the sensor resistance in air. C_{gas} denotes the concentration of the target being analyzed, β encapsulates the power characteristic specific to the sensor under consideration, and the proportionality constant K_{gas} varies depending on the nature of the analysis being conducted [27].

Table 1. The previous mox gas sensor mathematical models [5, 7, 22, 24, 25]

General gas sensor models	
$\delta(t) = \delta_1 e^{-t/\tau} + \delta_p e^{-t/\tau}(1-e^{-t/\tau}) + \delta_f(1-e^{-t/\tau})$	(1)
$R_{\text{gas}} = R_{\text{air}} \exp\left(B\left(\frac{1}{T_{\text{gas}}} - \frac{1}{T_{\text{air}}}\right)\right)$	(2)
$\frac{R}{R_0} = (1 + K_{\text{gas}} C_{\text{gas}})^{\beta}$	(3)
$Y = f(WX + b)$ & $R = f(c)$	(4)
$Y = A_0 + A_1 X + A_2 X^2 + A_3 X^3$	(5)
$f(x) = \text{sign}\left(\sum_{i=1}^{n} \alpha_i y_i K(x_i, x) + b\right),$	(6a)
$K(x_i, x) = \exp\left(-\gamma \lVert x_i - x \rVert^2\right)$	(6b)
$Y = A_0 + A_1 e^{-t/\tau_1} + A_2 e^{-t/\tau_2}$	(7)
If $R: H$, $\frac{\Delta R}{\Delta t} > 0$, $C:$ low, $\text{gas}_c: L$;	(8a)
If $R: L$, $\frac{\Delta R}{\Delta t} < 0$, $C:$ High, $\text{gas}_c: H$;	(8b)
If $R: M$, $\frac{\Delta R}{\Delta t}$: stable:M, $\text{gas}_c: M$	(8c)
$f(t) = \sum_{i=1}^{n} G_i e^{t/\tau_i}$	(9)
$\frac{d\Gamma}{dt} = k_{\text{ads}}\left(C_{\text{gas}} - \frac{\Gamma}{A}\right),$	(10a)
$\frac{d^2\Phi}{dx^2} = -\frac{1}{D}\frac{d\Phi}{dt},$	(10b)
$\Delta R/R_0 = k_r\left(\frac{\Gamma}{A}\right)\left(1 - \exp\left(-\frac{t}{\tau}\right)\right)$	(10c)
$G(T, N_z) = G_0 e^{-\frac{q^2 N_z^2}{2k\varepsilon_r \varepsilon_0 N_d T}}$	(11)

• **Artificial Neural Network (ANN) Model (Equation (4)):** The neural network model is a sophisticated machine learning paradigm designed to mimic the intricate structure and functionality of the human brain. Its application in gas sensor modeling involves predicting sensor responses based on a comprehensive set of input variables such as temperature, humidity, and the concentration of the target gas. By training the model with experimental data, its predictive accuracy can be significantly enhanced [30].

As shown in Equation (4) of Table 1, Y represents the output of the model, while X constitutes the input vector comprising sensor resistance values across different gas concentrations. The weight matrix W and bias vector b are crucial components determined during the model's training phase. The activation function f is then applied to generate the final output c, with the neural network continuously adjusting its weights and biases to minimize the disparity between predicted and actual outputs, as outlined in [31–33].

• **Polynomial Model (Equation (5)):** This equation is a polynomial model used to describe gas sensor responses based on polynomial terms (A_0, A_1, A_2, A_3). Here, Y signifies the disparity between the sensor's measured value and the baseline, while X represents the elapsed time from gas_{on} to gas_{off}, with X ranging from the initiation of gas_{on}. The coefficients designated with A in the fitted equations are subsequently utilized as parameters to characterize each

measurement. Parameter extraction and curve fitting are conducted on both the ascending (gas_{on}) and descending (gas_{off}) segments of the response curves.

• **Support Vector Machine (SVM) models (Equation (6)):** SVMs are frequently employed in gas sensor classification tasks, particularly for predicting gas concentrations. This model utilizes a non-linear classifier to infer gas concentration levels based on input variables such as sensor resistance, time constant, and gas concentration, specifically in the context of Mox gas sensors. The SVM model is represented by Eq. 6(a), where $f(x)$ signifies the output of the SVM classifier. In this equation, α_i and y_i represent the Lagrange multipliers and output labels, respectively. The kernel function $K(x_i, x)$ computes the similarity between the input data point x_i and the support vector x_i, while b denotes the bias term. The specific kernel function employed in this model is the Radial Basis Function (RBF), as depicted in Eq. 6(b), where γ acts as a tuning parameter controlling the width of the RBF kernel. This choice of kernel function is crucial for capturing non-linear relationships between input variables and achieving accurate gas concentration predictions. In a practical application, the proposed SVM model is utilized to detect three distinct types of gases (ethanol, acetone, and toluene) using a Mox gas sensor array. This approach aims to attain high accuracy in gas discrimination and superior performance compared to other machine learning algorithms [34–39].

• **Multi-Exponential Model (Equation (7)):** This equation presents a multi-exponential model used to capture complex sensor response behaviors with multiple decay constants (τ_1, τ_2).

• **Fuzzy Logic Model (Equation (8)):** The equation represents a fuzzy logic model used to forecast sensor responses based on input variables such as temperature, humidity, and gas concentration. This model can be trained using experimental data to enhance its predictive accuracy. The fuzzy logic model employs membership functions to characterize the degree of association of a gas concentration with a particular category. The model's output comprises linguistic variables that delineate the level of gas concentration, while the input variables encompass sensor Resistance (R), time constant ($\delta_R/\delta t$), and gas Concentration (C) [40]. The model can be described by the following principles: when sensor Resistance (R) is high with a positive change in ($\delta R/\delta t$), and gas Concentration (C) is low, the predicted gas concentration level is low. Conversely, when R is low with a negative change in (δ_R/δ_t), and C is high, the predicted gas concentration level is high. Finally, when R is medium, (δ_R/δ_t) is stable, and C is medium, the predicted gas concentration level is medium [40]. In a specific study, it is demonstrated that using a fuzzy logic model, an impressive accuracy of 89% can be achieved in predicting ammonia concentration in a Mox gas sensor array [40]. This highlights the efficacy of fuzzy logic in capturing complex relationships and making accurate predictions in gas sensing applications [41].

• **Exponential or Summation Model (Equation (9)):** This equation is a summation model used to combine multiple exponential terms to describe sensor responses. Where G_i denotes sample data, n represents the number of exponential terms, and τ_i signifies the time constant) emerges as one of the most viable models [42].

• **Dynamic Model (Equation (10)):** This type of gas sensor model takes into account the time-dependent behavior of gas sensors and the duration required for gas interaction with Mox materials. Various dynamic models have been proposed for Mox gas sensors, including those based on differential equations, data-driven neural networks, and hybrid models that integrate both approaches. Equation (10) of the model is founded on the concept that a sensor's response to a gas pulse can be delineated by two processes: adsorption and diffusion of the sensing material, enabling the prediction of the sensor's transient response to changes in gas concentration. For the adsorption process (Eq. 10(a)), Γ signifies the surface coverage of gas molecules on the sensing material, k_{ads} represents the adsorption rate constant, A denotes the surface area of the sensing material, and C_{gas} signifies the gas concentration in the surrounding environment. In the diffusion process (Eq. 10(b)), ϕ represents the gas concentration within the sensing material, x indicates the distance from the sensing layer, t represents time, and D represents the diffusion coefficient. The collective response of the sensor can be described as the change in resistance ($\Delta R/R_0$) over time, where R_0 is the initial resistance and ΔR is the change in resistance due to gas presence. The mathematical equation for this response is expressed in Eq. 10(c), incorporating the rate constant k_r for the gas sensing material reaction and the time constant for the diffusion process. This model enables the prediction of a Mox gas sensor's response under pulsed operation, providing valuable insights for optimizing gas sensing device design and performance [43, 44].

• **Surface Charge Model (Equation (11)):** In this equation, G_0 denotes the conductivity of the sensor, T represents the absolute temperature, σ denotes the surface charge density, k stands for Boltzmann's constant, q signifies the electrical

charge, N_d represents the density of ionized entities, and ε_r, ε_0 denote the permittivity constants. This equation enjoys widespread usage despite featuring numerous parameters and a sophisticated formulation [42].

The gas sensor modeling, as depicted in Table 1, encompasses previously proposed mathematical frameworks aimed at elucidating the intricate behavior of gas sensors, particularly in the realm of conductivity within the steady state domain. The selection of these models hinges upon the stability exhibited by sensor responses within this operational zone. The survey indicates that the Exponential Decay Model, Arrhenius Equation, Gas Concentration Model, Polynomial Model, Multi-Exponential Model, Exponential or Summation Model, and Surface Charge Model rely on empirical equations. In contrast, the dynamic model takes into account both physical and chemical processes [45], offering improved accuracy and sensitivity albeit at the cost of greater computational resources. The ANN model has also been found to be accurate but requires a large training dataset and computational [14–16]. The SVM model uses a non-linear classifier and has high accuracy but requires even a large dataset for training. The fuzzy logic model is useful in handling uncertain data but requires expert knowledge of rule-based systems [17, 46]. The accuracy of these models varies and is influenced by various factors. Selecting an appropriate model and calibration method is essential for achieving the desired accuracy and prediction time. It is generally recognized that a common problem among all the models for gas concentration detection is the consideration of numerous parameters [47], including the effects of temperature and humidity which can reduce the sensor speed [37]. In the Steady-state model, even the sensor response is modelled as a function of gas concentration using empirical equations. However, this model may not accurately capture the dynamic behaviour of the sensor and may be affected by temperature and humidity changes. The ANN model and SVM as advanced machine learning models are the popular approaches for gas sensor modelling, which has been found to be accurate in predicting the gas concentration levels and classification, with a prediction time of a few seconds to a few minutes. But those may require a large dataset and more computational resources compared to other models, SVM also needs a large dataset for model training [38]. The Fuzzy logic model may be useful in handling uncertain and imprecise data but requires expert knowledge in the form of rule-based systems [39]. The dynamic model considers the transient behaviour of the sensor response during gas exposure and incorporates physical and chemical processes involved in gas sensing [48], thus having numerous advantages compared to static models for Mox gas sensors. They can detect sudden changes in gas values and enhance the measurement process' s accuracy and reliability. However, environmental factors, sensing materials, and calibration techniques can affect their prediction time and accuracy [49–51].

2.3 *Problem statement*

More studies show that most of the researcher's attention absorb in the steady state area of gas sensors to have a stable response and some of them neglect the effect of dynamic temperature and humidity, but as it mentioned in various research transient response area contains various information that can be effective for more quick and accurate gas concentration detection [52]. The alternative approach (ANN, SVM, Dynamic), employing various modeling methods, aims to encompass the entire response curve. However, this comprehensive coverage may result in longer processing times and increased variability, particularly noticeable in Mox sensors that are sensitive to changes in temperature and humidity. Then based on importance of the transient time area In this research, emphasis is placed on the transient time area and the models derived from this specific region.

3. Methodology

3.1 *ENose data acquisition and sampling method*

In this research, data acquisition was conducted utilizing a purpose designed Enose [53] to sample the ethanol gas. The Electronic Nose, a sensor-dependent apparatus, emulates the olfactory capabilities of the human olfaction system, enabling the detection and identification of diverse odorous or chemical compounds. It harnesses an array of sensors to systematically dissect and categorize aromatic profiles, thereby extending its utility to multifarious domains, including but not limited to quality assurance, environmental surveillance, and advanced medical diagnostics [1]. To acquire data,

the acquisition system, as described in our previous research [54] (Figure 3), is designed using an Arduino based ENose platform. The system consists of four main components:

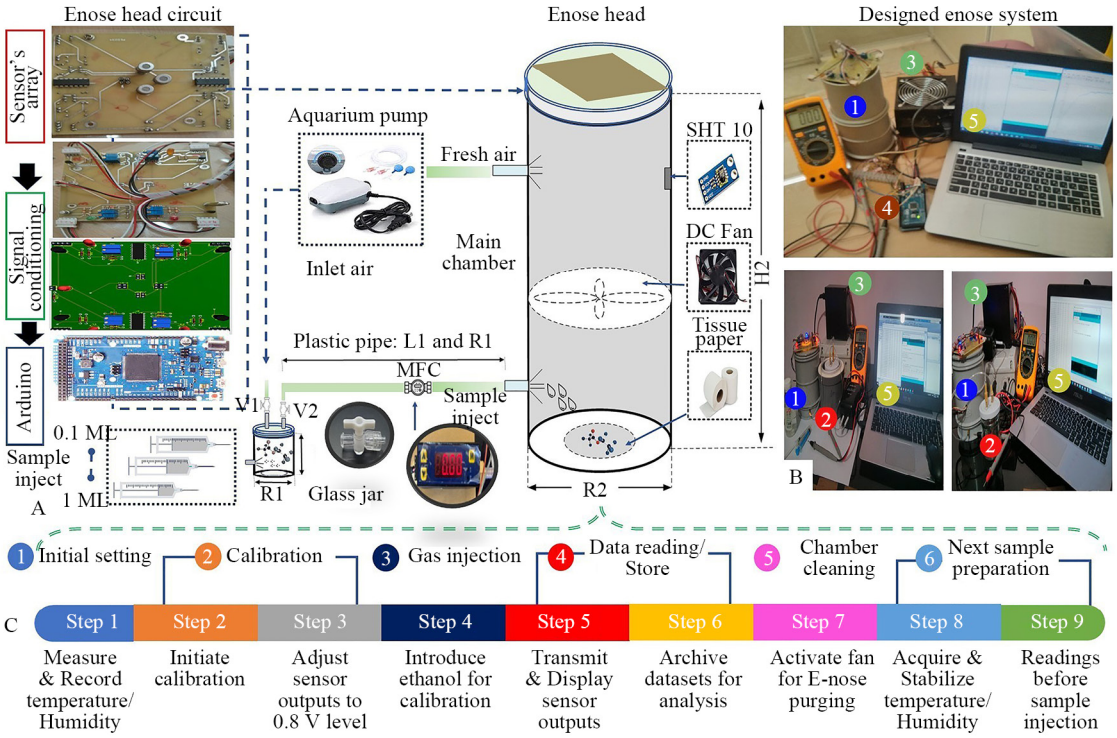

Figure 3. The Designed ENose part and sampling protocol. A: The designed ENose data acquisition system parts, B: The Design sections 1: Main chamber, 2: Glass jar, 3: Power supply, 4: Processor, 5: Personal Computer (PC), C: The sampling steps for gas sensor response

• **Ethanol Delivery System:** This system includes a glass jar (15 cm in height, 2.5 cm radius, total volume: 294.64 cm^3) with inlet and outlet valves, an aquarium pump (dual output, 3 W power, 4 L/min air output, 0.015 MPa pressure), and a plastic tube (50 cm in length, 0.1 cm radius, total volume: 1.57 cm^3) positioned close to the second part. A high-precision gas mass flow meter (MF4003, range: 0.1 to 5 SPLM) regulates airflow.

• **Main Chamber:**The main chamber consists of a PVC cylindrical pipe (50 cm in height, 7.5 cm radius total volume: 8839.256 cm^3) housing three MOX gas sensors (TGS 2620 with signal conditioning) and an SHT10 temperature sensor. The signal conditioning section employs a voltage divider circuit, where the MOX TGS 2620 functions as a variable sensing Resistor (Rs), adjusting its resistance in response to gas concentration changes. A 10 kΩ multi turn (R_L) acts as the load resistor, enabling fine tuned calibration. To improve sensitivity to low gas concentrations and ensure a stable signal before reaching the Analog-to-Digital Converter (ADC), an LM 324 operational amplifier is incorporated. The conditioned output is then transmitted to the processing section for sensor data acquisition. Additionally, the multi-turn resistor allows precise calibration, enhancing measurement accuracy. An Arduino Due board reads sensor values and transmits data to a computer via a serial connection at a baud rate of 9,600. The system is powered by a 12 V and 5 V power supply. The TGS 2620 sensor is ideal for alcohol detection due to its high sensitivity to ethanol vapors, wide detection range, and fast response time. It is also stable, cost effective, and easy to integrate into various applications [7]. Using three TGS 2620 gas sensors enhances accuracy by averaging data and providing redundancy if one sensor fails. It expands the detection range, improves response time, and reduces sensitivity to environmental factors. This setup ensures a more robust and efficient gas detection system.

• **Purging System:** This system includes a DC brushless fan (12 V, 0.5 A) and fresh air supplied from an additional output of the aquarium pump to purge and clean the chamber.

• **Data Logging and Analysis:** Sensor data is logged in CSV format and analyzed using MATLAB. As shown in Figure 3, the main tube contains a central fan and an electronic control board at one end, with the SHT10 sensor continuously monitoring temperature and humidity. A glass sampling tube connects the sample chamber to the main tube, and an air pump purges the system at a rate of 4 L/min. This airflow is regulated by a digital flow meter to maintain a controlled rate of 1.315 L/min, as calculated in Appendix Table 4.

Given the properties of Metal oxide semiconductor (Mox) sensors, the system is designed to respond quickly to temperature and humidity changes. However, ethanol measurements require calibration adjustments. Before determining ethanol concentrations, the sensor outputs are calibrated accordingly. Using an Arduino Due controller with a serial speed of 9600 bps, sensor data is recorded in csv format and analyzed in MATLAB (Figure 3).

Raw sensor data were recorded at 20 Hz using an Arduino Due (9,600 bps) and analyzed in MATLAB. Preprocessing included low pass filtering to remove high frequency noise, baseline correction by subtracting the pre-exposure mean, and outlier removal for spikes exceeding 3 standard deviations. Down sampling to 10 Hz was tested, which reduced computation time without affecting fit accuracy. These steps ensured stable signal by minimizing noise and drift effects. During ethanol preparation, liquid alcohol (0.1 to 1 mL) is injected into the ethanol delivery system via a syringe, and the ethanol ppm values are calculated (Appendix Table 5). The system's inlet and outlet airflow are adjusted to achieve the target ppm values, which are validated using a precise alcohol measurement tool (JY-C2H5OH, 12 V, range 0-500 PPM).

3.2 *The sampling protocol*

The sampling protocol is structured as follows: Initially, the prevailing temperature and humidity within the laboratory environment are measured and recorded. Subsequently, a calibration procedure is initiated based on predetermined temperature and humidity thresholds. During this process, the sensor outputs are adjusted to a standardized voltage level of 0.8 V. To facilitate calibration, a known quantity of ethanol is introduced into the chamber for each sampling iteration, measured in terms of parts per million (ppm). The resultant sensor output values are then transmitted and displayed on the processor board via the computer's serial port. These datasets are capable of being archived within the Excel environment and subjected to further in-depth analysis. Between successive experiments, the system activates a fan to purge the ENose and allow the sensors to return to an equilibrium state. Before commencing sample injection, temperature and humidity readings are acquired and stabilized, tailored to the specific experimental conditions [24, 25]. Mismatched heater temperatures can reduce both the sensitivity and specificity of gas sensors, making it difficult to obtain accurate and reliable measurements. Ensuring a stable and consistent heater temperature is crucial for optimal sensor performance, especially when precise detection of ethanol is required. Therefore, a calibration stage is conducted for all sampling processes to ensure accuracy. A total of 800 samples were collected across a concentration range of 60 to 400 ppm. This range is useful for early alcohol detection and, it holds relevance in industrial safety for detecting leaks and monitoring occupational exposure. In medical and ENose applications, it can aid in detecting alcohol presence in breath or the surrounding environment.

3.3 *Sample size calculation*

The computation of the sample size analysis was performed a priori using the software G-Power 3.1. We assumed an anticipated effect size (f) of 0.25, which is considered "medium". Assuming this effect size, the type I error of 0.05, and the power of 0.95, the required sample size was 84 for each of the three conditions. To be more conservative, we recorded more samples for each condition. Set 1 comprises 100 samples, testing ethanol density from 60 to 400 ppm at 27 °C with 30% humidity. Set 2 involves 400 samples, testing ethanol density from 60 to 400 ppm at 27 °C, 40 °C, 50 °C, and 60 °C, maintaining 30% humidity. In Set 3, over 300 samples (60 to 400 ppm) were collected, testing ethanol densities ranging from 20% to 50% at room temperature (27 °C) [55, 56].

4. A new space of functions as an universal approximator

In this segment, the aim is to delineate a novel functional domain while elucidating its cardinal property. The demonstration will show that this domain possesses the innate capacity to approximate any continuous non-linear function with infinitesimal error, thereby manifesting its universal approximation prowess. Considering X as a compact subset within $\mathbb{R}^n$. The definition of the Gaussian function space is articulated as follows:

$$G(\Delta) = \Big\{ \varphi(x) = \sum_{p=1}^{m} a_p \exp\Big(-\sum_{i=1}^{n} c_{ip}^2 (x_i - b_{ip})^2 \Big) : \\ a_p,\ c_{ip},\ b_{ip} \in \mathbb{R},\ x = (x_1,\ \ldots,\ x_n) \in \mathbb{R}^n,\ m \in \mathbb{N} \Big\}. \tag{1}$$

The subsequent theorem establishes that this space possesses the universal approximation capability.

Theorem 1 For any given continuous function $\psi(.)$ on compact setΔ in $\mathbb{R}^n$ and arbitrary $\varepsilon > 0$, there exists a function $\varphi(.) \in G(\Delta)$ such that $\sup_{x \in \Delta} |\psi(x) - \varphi(x)| < \varepsilon$.

Proof. By invoking the Stone-Weierstrass theorem ([57]), it suffices to demonstrate the following properties for the space $G(\Delta)$:

1. $G(\Delta)$ is an algebra, i.e. it is closed under addition, multiplication and scaler multiplication.
2. $G(\Delta)$ separates points on Δ, i.e. for any $\bar{x},\ \bar{y} \in \Delta,\ \bar{x} \neq \bar{y}$, there exists a function $\varphi_0(.) \in G(\Delta)$ such that $\varphi_0(\bar{x}) \neq \varphi_0(\bar{y})$.
3. $G(\Delta)$ vanishes at no point of Δ, i.e. for each $\bar{x} \in \Delta$ there is function $\varphi_0(.) \in G(\Delta)$ such that $\varphi_0(\bar{x}) \neq 0$.

To begin with, property (i) is proved. Let $\varphi_1(\cdot),\ \varphi_2(\cdot) \in G(\Delta)$. Then, they can be expressed as follows for any $x = (x_1,\ \ldots,\ x_m) \in \Delta$:

$$\varphi_1(x) = \sum_{p=1}^{\bar{m}} \bar{a}_p \exp\left(-\sum_{i=1}^{n} \bar{c}_{ip}^2 (x_i - \bar{b}_{ip})^2 \right) \tag{2}$$

$$\varphi_2(x) = \sum_{p=1}^{\hat{m}} \hat{a}_p \exp\left(-\sum_{i=1}^{n} \hat{c}_{ip}^2 (x_i - \hat{b}_{ip})^2 \right). \tag{3}$$

Then

$$\varphi_1(x) + \varphi_2(x) = \sum_{p=1}^{m} \alpha_p \exp\left(-\sum_{i=1}^{n} \gamma_{ip}^2 (x_i - \beta_{ip})^2 \right). \tag{4}$$

Where $m = \bar{m} + \hat{m}$ and

$$\alpha_p = \begin{cases} \bar{a}_p, & p = 1,\ \ldots,\ \bar{m} \\ \hat{a}_{p-\bar{m}}, & p = \bar{m}+1,\ \ldots,\ \bar{m}+\hat{m} \end{cases} \tag{5}$$

$$\beta_{ip} = \begin{cases} \bar{b}_{ip}, & p = 1, \ldots, \bar{m} \\ \\ \hat{b}_{i(p-\bar{m})}, & p = \bar{m}+1, \ldots, \bar{m}+\hat{m} \end{cases} \qquad i = 1, 2, \ldots, n \tag{6}$$

$$\gamma_{ip} = \begin{cases} \bar{c}_{ip}, & p = 1, \ldots, \bar{m} \\ \\ \hat{c}_{i(p-\bar{m})}, & p = \bar{m}+1, \ldots, \bar{m}+\hat{m} \end{cases} \qquad i = 1, 2, \ldots, n. \tag{7}$$

Hence $\varphi_1(x) + \varphi_2(x) \in G(\Delta)$. Also

$$\varphi_1(x) \times \varphi_2(x) = \sum_{\bar{p}=1}^{\bar{m}} \sum_{\hat{p}=1}^{\hat{m}} \bar{a}_{\bar{p}}\, \hat{a}_{\hat{p}} \exp\left(-\sum_{i=1}^{n} \left(\bar{c}_{i\bar{p}}^2 (x_i - \bar{b}_{i\bar{p}})^2 + \hat{c}_{i\hat{p}}^2 (x_i - \hat{b}_{i\hat{p}})^2 \right) \right). \tag{8}$$

Thus, it is trivial that $\varphi_1(x) \times \varphi_2(x) \in G(\Delta)$. Moreover, for any scalar $s \in \mathbb{R}$,

$$s\varphi_1(x) = \sum_{p=1}^{\bar{m}} s\bar{a}_p \exp\left(-\sum_{i=1}^{n} \bar{c}_{ip}^2 (x_i - \bar{b}_{ip})^2 \right), \quad x \in \Delta. \tag{9}$$

Thus, $s\varphi_1(x) \in G(\Delta)$. To demonstrate property (ii), consider $\bar{x},\ \bar{y} \in \Delta$, where $\bar{x} \neq \bar{y}$. By replacing $m = a_{i1} = c_{i1} = 1$ and $b_{i1} = \bar{x}_i$ for $i = 1,\ 2,\ ...,\ n$, the following function in $G(\Delta)$ can be obtained:

$$\varphi_0(x) = \exp\left(-\sum_{i=1}^{n} (x_i - \bar{x}_i)^2 \right) = \exp\left(-\|x - \bar{x}\|_2^2 \right),\ x \in \Delta. \tag{10}$$

For this function, $\varphi_0(\bar{x}) = 1$ and $\varphi(\bar{y}) = \exp\left(-|\bar{y} - \bar{x}|_2^2 \right)$. Since $\bar{x} \neq \bar{y}$, $\varphi_0(\bar{x}) \neq \varphi_0(\bar{y})$. Now, property (iii) is proven. Let $\bar{x} \in \Delta$ be given. For the function $\varphi 0(.) \in G(\Delta)$ defined by (10), $\varphi_0(\bar{x}) = 1 \neq 0$. Hence, $G(\Delta)$ does not vanish at any point of Δ. Note that in the special case where Δ is a compact set in $\mathbb{R}$, the space (1) can be expressed as

$$G(\Delta) = \left\{ \varphi(x) = \sum_{p=1}^{m} a_p \exp\left(-c_p^2 (x - b_p)^2 \right) : a_p,\ c_p,\ b_p \in \mathbb{R},\ x \in \Delta,\ m \in \mathbb{N} \right\}. \tag{11}$$

4.1 *Applying the space of Gaussian functions to control the sensor response (voltage)*

The space of Gaussian functions (11) will be applied to the problem given in Section 2. Here, three cases are considered.

4.1.1 *Case I: Temperature and humidity are fixed and gas is changed*

In this case, the following set of data for fixed Temperature $T = T_0$ and humidity $H = H_0$ is assumed to be available from the system through measuring tools at time interval $[0,\ \tau]$:

$$\left\{(\bar{g}_j,\ \bar{v}_{je}) : j = 1,\ 2,\ ...,\ J,\ e = 1,\ 2,\ ...,\ E\right\}. \tag{12}$$

Where $\bar{v}_{je}$ denotes the measured voltage at time $0 \le t = t_e \le \tau$ for the injected gas $g = \bar{g}_j$. Leveraging this data and the universal approximation capability of the space of functions defined by (1), the following continuous function is suggested to approximate the output voltage of the system based on the injected gas $g = \bar{g}_j$:

$$v_j(t) = \sum_{p=1}^{m} a_{pj} \exp\left(-{c_{pj}}^2 (t - b_{pj})^2\right),\ j = 1,\ 2,\ ...,\ J. \tag{13}$$

Where for any $j = 1,\ 2,\ ...,\ J$, parameters $(a_{pj},\ b_{pj},\ c_{pj}),\ p = 1,\ 2,\ ...,\ m$ can be calculated by solving the following nonlinear algebraic system.

$$\bar{v}_{je} - \sum_{p=1}^{m} a_{pj} \exp\left(-{c_{pj}}^2 (t_e - b_{pj})^2\right) = 0,\ e = 1,\ 2,\ ...,\ E. \tag{14}$$

This system can be solved with respect to the $(a_{pj},\ b_{pj},\ c_{pj}),\ p = 1,\ 2,\ ...,\ m$ by quasi-Newton methods such as Levenberg-Marqurdt method. Moreover, the following least square minimization problem can be solved for any $j = 1,\ 2,\ ...,\ J$:

$$\underset{a_{pj},\ b_{pj}c_{pj}}{Minimize} \quad R = \sum_{e=1}^{E} \left[\bar{v}_{je} - \sum_{p=1}^{m} a_{pj} \exp\left(-{c_{pj}}^2 (t_e - b_{pj})^2\right)\right]^2. \tag{15}$$

Now, to approximate the sensor response for an arbitrary gas concentration g (within the measured range), rather than only the discrete concentrations $\bar{g}_j$, an interpolation across the concentration domain is required. Using the functions $v_j(t)$ from Eq. (13), which model the response at specific concentrations $\bar{g}_j$, we construct a continuous function over g via Lagrange interpolation:

$$v(t; g) = \sum_{j=1}^{J} v_j(t) L_j(g), \quad 0 \le t \le \tau, \tag{16}$$

where $L_j(g) = \prod_{r=1,\ r \ne j}^{J} \dfrac{g - g_r}{g_j - g_r}$ is the Lagrange basis polynomial. This method was chosen because it provides an exact fit at the pre-calculated points $v_j(t)$ and offers a simple way to create a smooth, continuous model over the gas concentration variable. This allows us to estimate the voltage response for any concentration g between 60 and 400 ppm.

4.1.2 *Case II: Humidity is fixed and, temperature and gas PPM are changed*

In this case, we assume that the following set of data for fixed humidity $H = H_0$ is available from the system by measuring tools at time interval $[0,\ \tau]$

$$\left\{(\bar{g}_j,\ \bar{T}_k,\ \bar{v}_{jke}) : j = 1,\ 2,\ ...,\ J;\ k = 1,\ 2,\ ...,\ K\ ; e = 1,\ 2,\ ...,\ E\right\}, \tag{17}$$

where $\bar{v}_{jke}$ is the measured voltage at time $0 \leq t = t_e \leq \tau$ for the injected gas $g = \bar{g}_j$ and temperature $T = \bar{T}_k$. The same as above-mentioned approach, by these data and the universal approximation capability of space of functions defined by (1), the output voltage of system according to injected gas $g = \bar{g}_j$ and temperature $T = \bar{T}_k$ can be approximated by the following continuous function:

$$\bar{v}_{jk}(t) = \sum_{p=1}^{m} \bar{a}_{pjk} \exp\left(-\bar{c}_{pjk}{}^2 (t - \bar{b}_{pjk})^2\right), \; j = 1, \, 2, \, ..., \, J. \tag{18}$$

where for any $j = 1, \, 2, \, ..., \, J$ and $k = 1, \, 2, \, ..., \, K$, the parameters $\left(\bar{a}_{pjk}, \, \bar{b}_{pjk}, \, \bar{c}_{pjk}\right), \; p = 1, \, 2, \, ..., \, m$ can be calculated by solving the following nonlinear algebric system.

$$\bar{v}_{jke} - \sum_{p=1}^{m} \bar{a}_{pjk} \exp\left(-\bar{c}_{pjk}{}^2 (t_e - \bar{b}_{pjk})^2\right) = 0, \; e = 1, \, 2, \, ..., \, S. \tag{19}$$

Moreover, the following least square minimization for any $j = 1, \, 2, \, ..., \, j$ and $k = 1, \, 2, \, ..., \, K$ can be solved:

$$\underset{\bar{a}_{pj}, \, \bar{b}_{pj}, \, \bar{c}_{pj}}{Minimize} \quad W = \sum_{e=1}^{S} \left[\bar{v}_{jke} - \sum_{p=1}^{m} \bar{a}_{pjk} \exp\left(-\bar{c}_{pjk}{}^2 (t_e - \bar{b}_{pjk})^2\right) \right]^2. \tag{20}$$

Now, the sensor response with respect to the injected gas g and temperature T can be interpolated as :

$$v(t; \, g, \, T) = \sum_{k=1}^{K} \sum_{j=1}^{J} v_{jk}(t) \bar{L}_j(g) \bar{L}_k(T), \; 0 \leq t \leq \tau, \tag{21}$$

where $L_j(g) = \prod_{r=1, \, r \neq j}^{D} \dfrac{g - g_r}{g_j - g_r}$ and $L_j(T) = \prod_{r=1, \, r \neq k}^{D} \dfrac{T - T_r}{T_k - T_r}$ are the Lagrange multiplier. Note that $v(t; \, g_j, \, T_k) = v_{jk}(t)$.

4.1.3 *Case III: Temperature is fixed and, humidity and gas are changed*

In this case, the following set of data for fixed humidity $T = T_0$ is assumed to be available from the system through measuring tools at time interval $[0, \, \tau]$:

$$\left\{ (\bar{g}_j, \, H_l, \, \bar{v}_{jle}) : j = 1, \, 2, \, ..., \, J; \, l = 1, \, 2, \, ..., \, L; \, e = 1, \, 2, \, ..., \, E \right\}. \tag{22}$$

Where $\bar{v}_{jle}$ represents the measured voltage at time $0 \leq t = te \leq \tau$ for the injected gas $g = \bar{g}j$ and temperature $H = \bar{H}l$. By a similar process as case II, can get.

$$\hat{v}_{jl}(t) = \sum_{p=1}^{m} \hat{a}_{pjl} \exp\left(-\hat{c}_{pjl}{}^2 (t - \hat{b}_{pjl})^2\right), \; e = 1, \, 2, \, ..., \, S. \tag{23}$$

$$\hat{v}(t;\, g,\, H) = \sum_{l=1}^{L} \sum_{j=1}^{K} \hat{v}_{jl}(t) L_j(p) \hat{L}_l(H), \quad 0 \le t \le \tau. \tag{24}$$

In the next section, the aforementioned approach will be simulated using data obtained from the system.

5. Model verification result

To validate the proposed model, the next step includes verifying it with three different sets of data. These data sets are used to simulate our approach and show case how the sensor responds in various scenarios. Note that solving the nonlinear algebraic systems (13) and (19) is equivalent to solving the optimization problems (14) and (20), respectively. To solve these systems, we used the Levenberg-Marquardt algorithm, a quasi-Newton method. This was implemented using the fsolve command in MAT- LAB, with the algorithm specified in the options. The numerical results for the approximation coefficients were thus obtained by solving the corresponding algebraic systems with the Levenberg-Marquardt algorithm. All simulations were run in MATLAB 2020a on a PC with an Intel(R) Core(TM) i5-1035G1 CPU @ 1.19 GHz. The CPU time required to obtain all computational results in this section for $m \le 15$ was about 1-3 seconds, which is considered acceptable for this modeling purpose. Based on our experimental results, it was found that, for this gas sensor response problem, using $m \le 15$ is sufficient to obtain relatively good and acceptable approximations.

5.1 *Case I: fixed temperature and humidity*

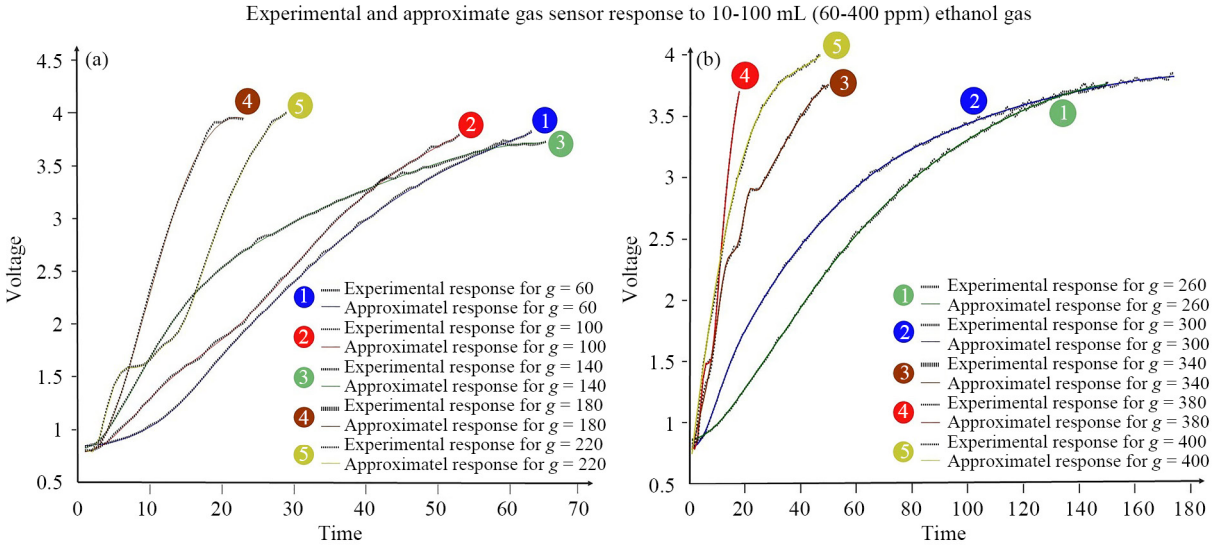

Figure 4. Sensor response in Case I. (a) for $g = 60,\ 100,\ 140,\ 180,\ 220$ ppm, 1) Experimental response and approximate response for $g = 60$, 2) Experimental and approximate response for $g = 100$, 3) Experimental and approximate response for $g = 140$, 4) Experimental and approximate response for $g = 180$, 5) Experimental and approximate response for $g = 220$. (b) for $g = 260,\ 300,\ 340,\ 380,\ 400$ ppm. 1) Experimental and approximate response for $g = 260$, 2) Experimental and approximate response for $g = 300$, 3) Experimental and approximate response for $g = 340$, 4) Experimental and approximate response for $g = 380$, 5) Experimental and approximate response for $g = 400$

In the first case of experiment data, the sensor response was collected over time $t = 1,\ 2,\ \ldots,\ 250$ seconds for injected gas concentrations of $g = 60,\ 100,\ \ldots,\ 400$ parts per million (ppm), with a constant temperature of $T = 27$ degrees Celsius and humidity level of $H = 30\%$. Figure 4 displays the results of the fitted model (relation (13)) compared

to the real sensor response in the transient time region. As the Figures 4 demonstrate that the experimental response can be accurately approximated using a set of Gaussian functions. The fitted data indeed showcases the model's ability to accurately represent real sensor data. The close match between the curves indicates how effectively our model captures the dynamics and characteristics of the actual sensor response. For instance, the data corresponding to $g = 140$ is presented in Table 2, which indicates that the output response, calculated using Formula (13), as the case, the continuous approximate response $v_3(t)$ in relation (25) can be expressed as follows:

$$v_3(t) = \sum_{p=1}^{12} a_{p3} \exp\left(-{c_{p3}}^2 (t - b_{p3})^2\right), \; t \geq 1. \tag{25}$$

Table 2. Experimental data (or real dataset) corresponding to $g = 140$, Temperature = 27 °C, Humidity = 30%, Time (T) in second (s), Sensor Response (SR) in Voltage (V)

T (s)	SR (V)	T (s)	SR (V)	T (s)	SR (V)	T (s)	SR (V)
1	0.83	17	2.35	33	3.06	49	3.49
2	0.85	18	2.41	34	3.10	50	3.51
3	0.89	19	2.48	35	3.13	51	3.54
4	0.98	20	2.54	36	3.17	52	3.56
5	1.09	21	2.59	37	3.19	53	3.58
6	1.21	22	2.65	38	3.22	54	3.60
7	1.32	23	2.70	39	3.25	55	3.63
8	1.44	24	2.73	40	3.27	56	3.64
9	1.56	25	2.81	41	3.30	57	3.67
10	1.68	26	2.84	42	3.36	58	3.71
11	1.80	27	2.85	43	3.39	59	3.71
12	1.90	28	2.89	44	3.38	60	3.70
13	2.01	29	2.93	45	3.44	61	3.70
14	2.10	30	2.97	46	3.43	62	3.71
15	2.20	31	3.01	47	3.45	63	3.70
16	2.28	32	3.04	48	3.49	64	3.71

Table 3. Coefficients of the approximate continuous response (17) for Case I, with $g = 140$ ppm and $p = 1, 2, \ldots, 12$

p	$a_{p3},\ p$	$b_{p3},\ p$	$c_{p3},\ p$
1	4.149675	5.099806	0.064896
2	7.213591	-15.7653	0.01683
3	5.806106	-13.9111	0.016269
4	-2.13023	-5.39761	0.01953
5	-11.1424	-1.46921	0.017349
6	-9.87165	-0.92902	0.05254
7	-2.73543	-10.5128	0.021356
8	6.785903	-15.5015	0.017187
9	-10.1322	-2.13814	0.017149
10	-11.0638	-1.51845	0.017332
11	6.986078	-15.4259	0.016652
12	19.5055	-16.1829	0.011308

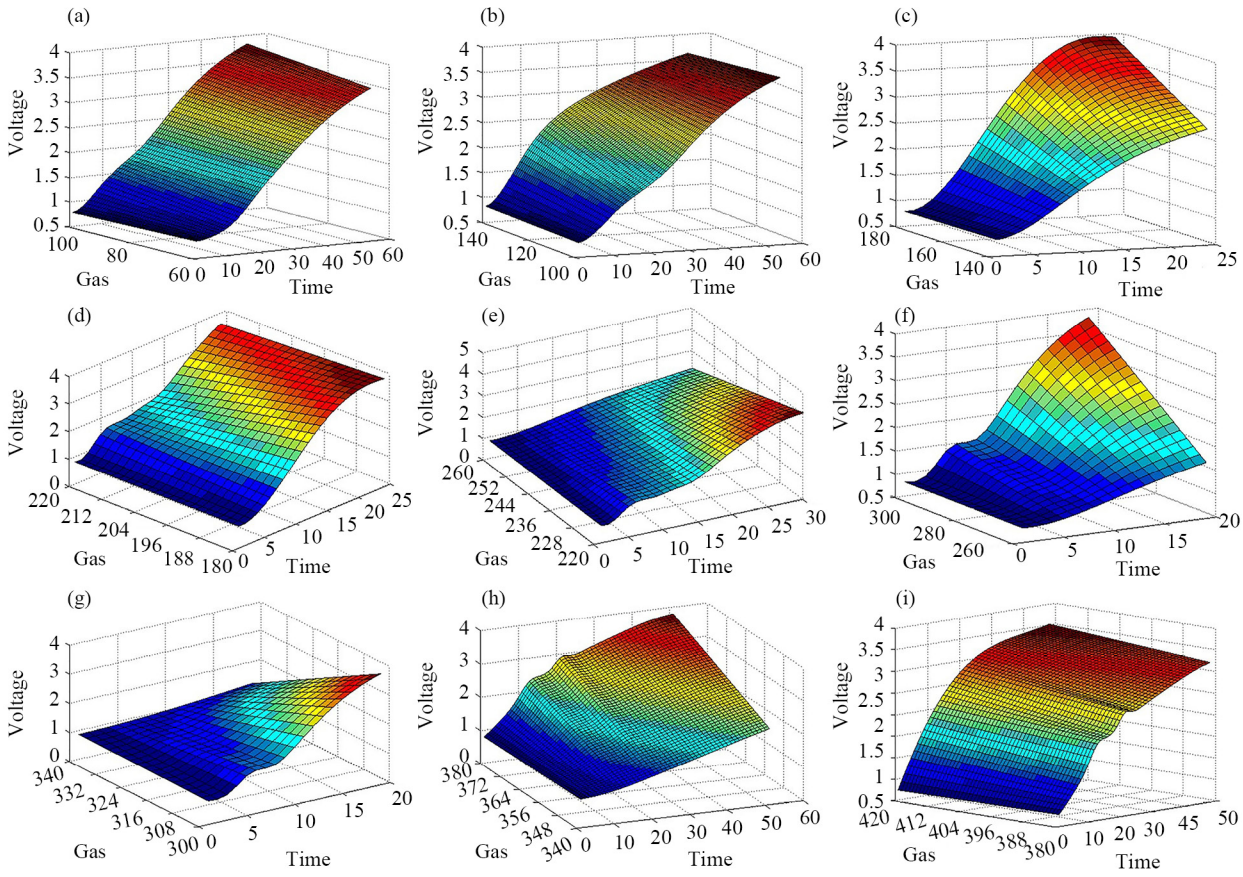

Figure 5. Sensor response for in Case I. The response of system with respect to the time for Case I. (a) gas $g \in [60, 100]$, (b) gas $g \in [100, 140]$, (c) gas $g \in [140, 180]$, (d) gas $g \in [180, 220]$, (e) gas $g \in [220, 260]$, (f) gas g $g \in [260, 300]$, (g) gas $g \in [300, 340]$, (h) gas $g \in [340, 380]$, (i) gas $g \in [380, 400]$

The coefficients (a_{p3}, b_{p3}, c_{p3}), where $p = 1, 2, \ldots, 12$, are provided in Table 3 for reference of the Case I. Additionally, the goal is to approximate the sensor responses for specific injected gas concentrations. To achieve this, the interpolations obtained from relation (8) are utilized. The resulting approximate responses are visualized in Figure 5. The Figure 5 illustrates that within the range of discrete data points from 60 to 400, the model effectively generates continuous values, seamlessly bridging the gaps between these data points. This point facilitates the differentiation and extraction of Voltage, Gas ppm, and time values from each other. It's important to note that these values were not directly measured but rather estimated by the model. Figure 6 illustrates the model's capability to successfully estimate and display the gas response during transient time. This aspect aids in distinguishing and separating Voltage, Gas ppm, and time values.

For example, Figure 6 showcases the estimated gas response at ppm levels of 100, 180, 260, and 340. It's important to note that these values were estimated by the model, demonstrating its ability to successfully predict and display responses during transient time.

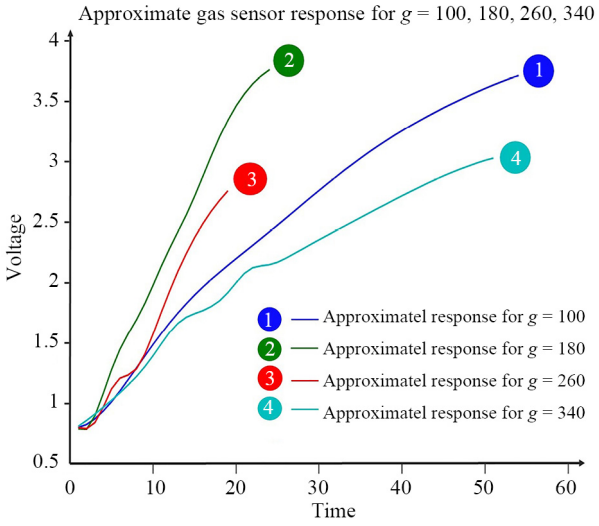

Figure 6. Approximate sensor response for gas $g = 100,\ 180,\ 260,\ 340$ ppm in Case I. 1) Approximate response for $g = 100$, 2) Approximate response for $g = 180$, 3) Approximate response for $g = 260$, 4) Approximate response for $g = 340$

5.2 *Case II: change the temperature and fixed the humidity*

In the second experiment, the sensor response was collected over time $t = 1,\ 2,\ ...,\ 250$ seconds for injected gas concentrations of $g = 340,\ 380$ parts per million (ppm), with temperatures of $T = 40\ ^\circ\text{C},\ 50\ ^\circ\text{C},\ 60\ ^\circ\text{C}$, and a fixed humidity of $H = 30\%$. Figures 7 display the experimental sensor responses alongside their corresponding approximations, as denoted by relation (11).

As it shown in Figure 7, the experimental response can be accurately approximated. Furthermore, to check the model functionality for the data which is not sampled in real the Figure 8 shown the approximate the sensor response for specific injected gas concentrations $g = 328,\ 336,\ 344,\ 354$ ppm and a temperature of $T = 40\ ^\circ\text{C}$.

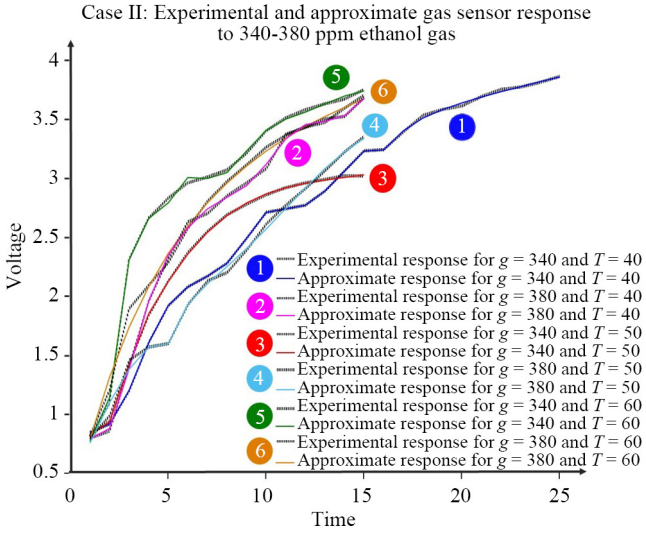

Figure 7. Sensor response for g=340, 380 ppm and $T = 40\ ^\circ\text{C},\ 50\ ^\circ\text{C}$, and $60\ ^\circ\text{C}$ in Case II. 1) Experimental and approximate response for $g = 340$ and $T = 40$, 2) Experimental and approximate response for $g = 380$ and $T = 40$, 3) Experimental and approximate response for $g = 340$ and $T = 50$, 4) Experimental and approximate response for $g = 380$ and $T = 50$, 5) Experimental and approximate response for $g = 340$ and $T = 60$, 6) Experimental and approximate response for $g = 380$ and $T = 60$

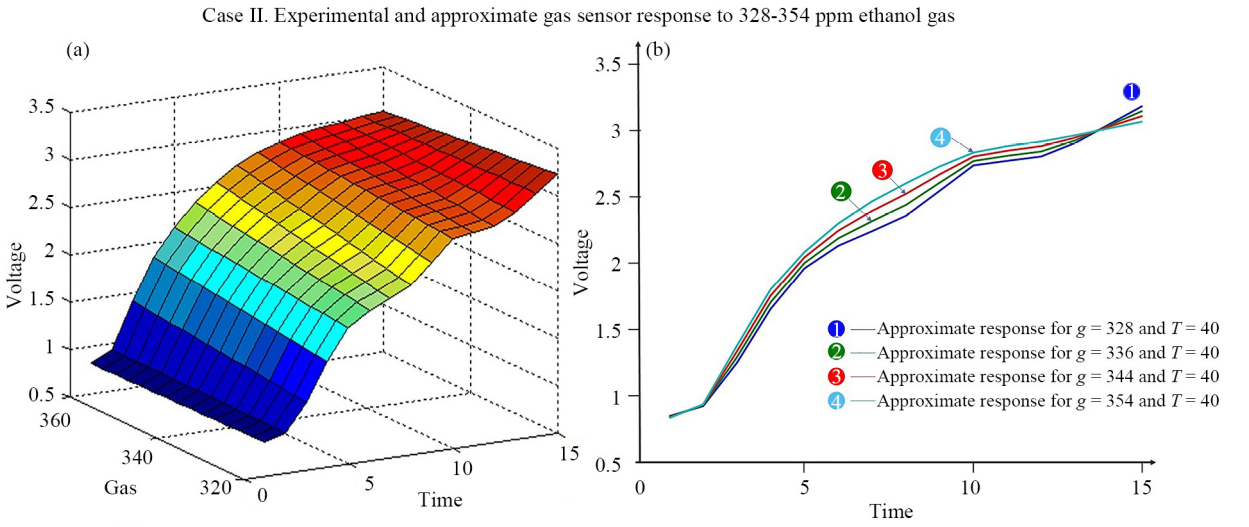

Figure 8. (a): The response of the system with respect to the time t and gas $g \in [340,\ 380]$ for $T = 27$ °C in Case II. (b): Approximate sensor response for different injected gas g and temperature ($T = 40$ °C) in Case II. 1) Experimental and approximate response for $g = 328$ and $T = 40$, 2) Experimental and approximate response for $g = 336$ and $T = 40$, 3) Experimental and approximate response for $g = 344$ and $T = 40$, 4) Experimental and approximate response for $g = 354$ and $T = 40$

5.3 *Case III: change the humidity and fixed the temperature*

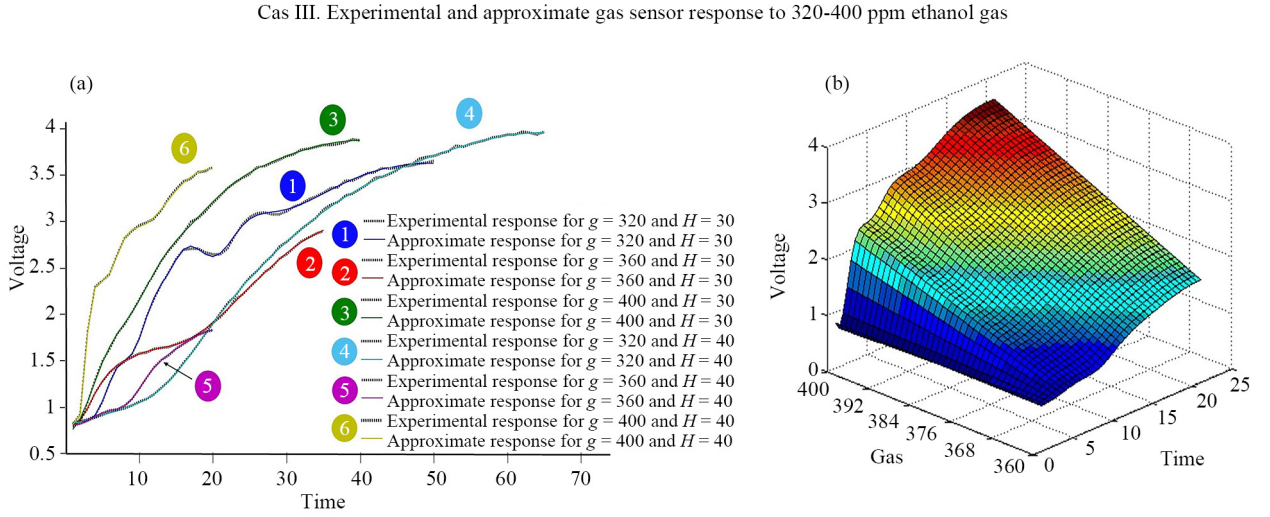

Figure 9. (a) Sensor response for different injected gas and humidity, with fixed temperature ($T = 27$ °C) in Case III. 1) Experimental and approximate response for $g = 320$ and $H = 30$, 2) Experimental and approximate response for $g = 360$ and $H = 30$, 3) Experimental and approximate response for $g = 400$ and $H = 30$, 4) Experimental and approximate response for $g = 320$ and $H = 40$, 5) Experimental and approximate response for $g = 360$ and $H = 40$, 6) Experimental and approximate response for $g = 400$ and $H = 40$. (b) The response of the system with respect to time t and gas $g \in [380, 400]$ for $H = 40\%$ in Case III

In the third experiment, the sensor response was collected over time $t = 1,\ 2,\ \ldots,\ 250$ seconds for injected gas concentrations of $g = 340,\ 380,\ 400$ parts per million (ppm), with humidity levels $H = 30\%, 40\%$, and a fixed temperature of $T = 27$ °C. Figure 9a, display the experimental sensor responses alongside their corresponding approximations, as

denoted by relation (16). To calculate the response concerning time and gas variables, relation (17) is utilized for intervals and illustrated in Figure 9b.

5.4 *Model comparison*

The next step in demonstrating the efficiency of the proposed model is to compare the suggested Gaussian approximation with the exponential (Table 1: Equation (5)) and polynomial (Table 1: Equation (9)) approximations. Exponential and polynomial models for gas sensors offer unparalleled flexibility in capturing a wide range of sensor responses, making them adaptable to various gas detection scenarios.

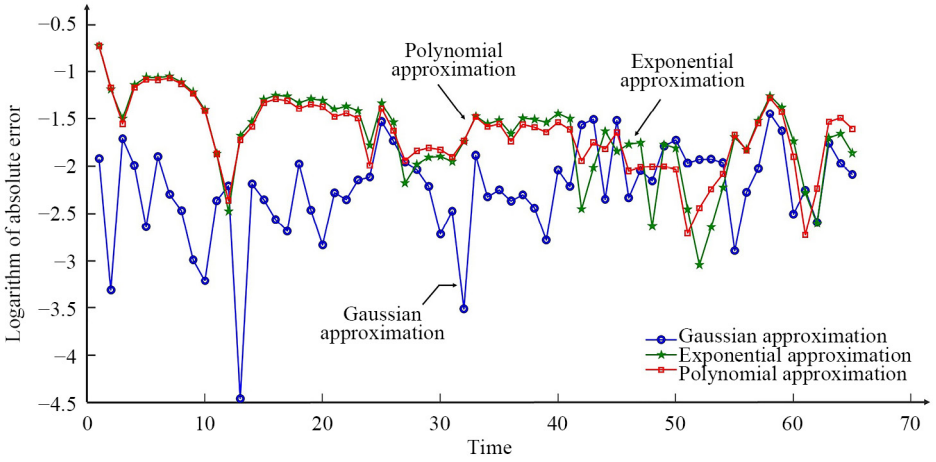

Figure 10. The proposed Gaussian model approximation Vs polynomial and exponential model

They excel at representing non-linear relationships commonly found in gas sensor responses, allowing for fine-tuning and customization to specific gas detection requirements, thus enhancing accuracy and sensitivity. Additionally, these models enable interpolation between known data points, improving overall detection capabilities, all while maintaining mathematical simplicity, aiding in their implementation and computational efficiency. This comparison is facilitated using the following Absolute Error (AE) and Total Error (TE):

$$TE = \sqrt{\sum_{e=1}^{R} |\bar{v}(t_e) - v(t_e)|^2}, \quad AE(t_e) = |\bar{v}(t_e) - v(t_e)|, \quad e = 1, 2, \ldots, E. \tag{26}$$

Where $v(t)$ and $\hat{v}(t)$ are the experimental voltage and obtained approximate voltage at time t. The logarithm of the absolute error (i.e., $\log_{10}(AE)$) for the suggested Gaussian approximation, exponential approximation (model (9) in Table 1), and polynomial approximation (model (7) in Table 1) are presented in Figure 10. As depicted in Figure 10, it can be seen that the suggested approach is more accurate than the two other methods. Also, the Total Errors (TEs) for the suggested Gaussian approximation, exponential approximation (model (9) in Table 1), and polynomial approximation (model (7) in Table 1) are 0.0978, 0.3532, and 0.3378, respectively, showing the superiority of the suggested Gaussian approximation in approximating the gas sensor response. The number of components (m) was selected to balance model fidelity with generalization ability and to avoid overfitting. The Total Error (TE) was calculated for different values of m. The results, summarized in the new Figure 11, show that the TE on the validation set decreases sharply as m increases from 2 to 12. For $m > 12$, the validation error no longer improves and even begins to increase slightly due to overfitting, while the training error continues to decrease. Therefore, $m = 12$ was chosen as the optimal complexity for our model in

Case I, as it provides an excellent fit to the training data while maintaining strong generalization performance on unseen data. This value was used consistently for all concentrations in Case I to ensure a fair comparison.

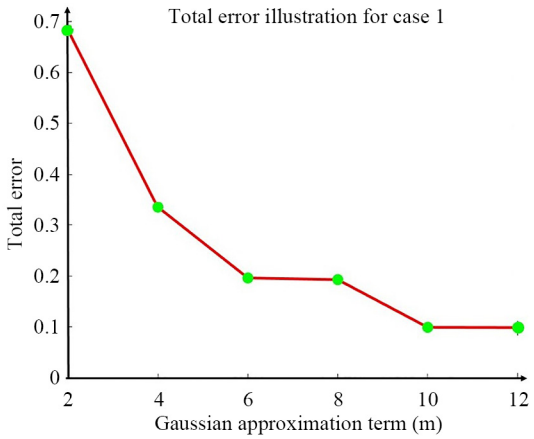

Figure 11. Decreasing total error with increasing number of Gaussian approximation terms

6. Conclusions and suggestions

Mox sensors are crucial due to their wide gas detection range, affordability, and suitability for compact, real time monitoring systems. Then Modeling MOX sensors enable predictive analysis for diverse gas responses, facilitate calibration and drift correction, and optimize sensor design for enhanced performance and system integration. The previous review study highlights that Mox gas sensors consist of five parts, with the response curve and steady state segment commonly used for modeling, sensitive to temperature and humidity. Contrarily, the transient time section is less influenced by environmental factors.

This research centers on employing Gaussian mathematical equations to model the transient time section of Mox gas sensors. It investigates how these sensors respond to changes in temperature and humidity across three distinct scenarios (case I-III) using real sample data, with a particular focus on studying ethanol odor at varying concentrations. The chosen model is selected based on its inherent nature and similarity in shape to the sensor response. It has the potential to be extended to cover the entire sensor response range effectively. The Gaussian function offers smooth, continuous modeling suitable for various data transitions. Its mathematical simplicity aids computational efficiency and easy manipulation in models. Central Limit Theorem relevance makes it valuable for statistical analysis and random processes. Widely applicable in fields like physics, engineering, and machine learning. Flexible properties allow tailored models for specific data characteristics and requirements. The results obtained demonstrate the proposed model's ability to accurately fit real sensor data and estimate gas sensor concentrations, as well as temperature and humidity values. Additionally, a comparison with commonly available models (exponential approximation and polynomial approximation), with lower AE and TE values, the Gaussian approximation demonstrates superior accuracy in approximating the gas sensor response compared to the other two models. These two models were selected based on their ability to capture complex sensor responses and provide customized solutions that make exponential and polynomial models are essential in gas sensor modeling and analysis. While the proposed Gaussian-based model effectively captures the transient behavior of the TGS 2620 sensor for ethanol detection, it has some limitations. Increased computational complexity with larger datasets or multiple environmental variables may affect real-time implementation, and extending the model to other gases or sensor types may require additional calibration or re-parameterization. Addressing these limitations represents a direction for future work. Future work will focus on extending the proposed Gaussian transient model beyond ethanol to additional gases such as propanol and ammonia, and to multi-component atmospheres. We plan to develop multi-Gaussian fitting and deconvolution strategies for mixture modeling, and investigate sensor drift and aging to assess parameter stability

and the need for periodic recalibration or online adaptation. In parallel, alternative mathematical formulations will be explored to improve modeling accuracy. We also aim to adapt the model for real-time and embedded ENose systems by optimizing algorithms for low-power micro controllers and streamlining code implementation. These efforts will enhance the generalizability, robustness, and practical applicability of the framework in industrial monitoring, environmental sensing, and healthcare diagnostics.

Author's contribution

Ata Jahangir Moshayedi (AJM), Mohammad Hadi Noori Skandari (MHNS), Jiandong Hu (J.H), Abolfazl Razi (A.R), David Bassir (DB). Conceptualization: AJM, MHNS, J.H, A.R and D.B; Data curation: AJM, MHNS, J.H and D.B; Visualization, Software, Investigation: AJM, MHNS, A.R and D.B; Writing-original draft preparation: AJM, MHNS, A.R and D.B; Writing-review and editing: AJM, MHNS, J.H, A.R, and D.B; All authors have read and agreed to the published version of the manuscript.

Acknowledgments

Acknowledgments: The authors would like to thank RARL (Robotic Automation Research Lab, School of Information Engineering, Jiangxi University of Science and Technology, No. 86, Hongqi Ave., Ganzhou 341000, China.

Funding

This work was supported by Smart Structural Health Monitoring and Control Laboratory, DGUT-CNAM, Dongguan University of Technology, China

Data availability statement

The data used to support the findings of this study are available from the corresponding author upon request.

Conflict of interest

The authors declare that they have no known competing financial interests or personal relationships that could have appeared to influence the work reported in this paper.

References

[1] Moshayedi AJ, Khan AS, Yang S, Geng K, Hu J, Soleimani M, et al. E-nose design and structures from statistical analysis to application in robotic: A compressive review. *EAI Endorsed Transactions on AI and Robotics*. 2023; 2: 1-20. Available from: https://doi.org/10.4108/airo.v2i1.3056.

[2] Moshayedi AJ, Khan AS, Hu J, Nawaz A, Zhu J. E-nose-driven advancements in ammonia gas detection: A comprehensive review from traditional to cutting-edge systems in indoor to outdoor agriculture. *Sustainability*. 2023; 15(15): 11601. Available from: https://doi.org/10.3390/su151511601.

[3] Chen D, Miao Z, Peng M, Xing H, Zhang H, Teng X. The co-expression of circRNA and mRNA in the thymuses of chickens exposed to ammonia. *Ecotoxicology and Environmental Safety*. 2019; 176: 146-152. Available from: https://doi.org/10.1016/j.ecoenv.2019.03.076.

[4] Marinković Z, Gugliandolo G, Latino M, Campobello G, Crupi G, Donato N. Characterization and neural modeling of a microwave gas sensor for oxygen detection aimed at healthcare applications. *Sensors*. 2020; 20(24): 7150. Available from: https://doi.org/10.3390/s20247150.

[5] Li D, Xu X, Li Z, Wang T, Wang C. Detection methods of ammonia nitrogen in water: A review. *TrAC Trends in Analytical Chemistry*. 2020; 127: 115890. Available from: https://doi.org/10.1016/j.trac.2020.115890.

[6] Moshayedi AJ, Gharpure DC. Evaluation of bio inspired Mokhtar: Odor localization system. In: *2017 18th International Carpathian Control Conference (ICCC)*. Sinaia, Romania: IEEE; 2017. p.527-532. Available from: https://doi.org/10.1109/CarpathianCC.2017.7970457.

[7] Moshayedi AJ, Kazemi E, Tabatabaei M, Liao L. Brief modeling equation for metal-oxide; TGS type gas sensors. *Filomat*. 2020; 34(15): 4997-5008. Available from: https://doi.org/10.2298/FIL2015997M.

[8] Bulbul A, Kim H. PPB level gas quantification by bubble chromatography. In: *2017 19th International Conference on Solid-State Sensors, Actuators and Microsystems (TRANSDUCERS)*. Kaohsiung, Taiwan: IEEE; 2017. p.660-663. Available from: https://doi.org/10.1109/TRANSDUCERS.2017.7994135.

[9] Kumar A, Kashyap R, Kumar R, Singh R, Prasad B, Kumar M, et al. Experimental and numerical modelling of a nanostructured nickel ferrite-based ammonia gas sensor. *Journal of Electronic Materials*. 2022; 51(7): 4040-4053. Available from: https://doi.org/10.1007/s11664-022-09673-w.

[10] Raza M, Chen Y, Trapp J, Sun H, Huang X, Ren W. Smoldering peat fire detection by time-resolved measurements of transient CO_2 and CH_4 emissions using a novel dual-gas optical sensor. *Fuel*. 2023; 334: 126750. Available from: https://doi.org/10.1016/j.fuel.2022.126750.

[11] Binson VA, George MM, Sibichan MA, Raj M, Prasad K. Freshness evaluation of beef using MOS based E-Nose. In: *2023 International Conference on Intelligent Data Communication Technologies and Internet of Things (IDCIoT)*. Bengaluru, India: IEEE; 2023. p.792-797. Available from: https://doi.org/10.1109/IDCIoT56793.2023.10053399.

[12] Zhang Z, Zhou Q, Qiu S, Zhou J, Huang J. Efficient monitoring of microbial communities and chemical characteristics in incineration leachate with electronic nose and data mining techniques. *Chemosensors*. 2023; 11(4): 229. Available from: https://doi.org/10.3390/chemosensors11040229.

[13] Binson VA, Subramoniam M, Mathew L. Detection of COPD and Lung Cancer with electronic nose using ensemble learning methods. *Clinica Chimica Acta*. 2021; 523: 231-238. Available from: https://doi.org/10.1016/j.cca.2021.10.005.

[14] Binson VA, Thomas S, Subramoniam M. Non-invasive detection of early-stage lung cancer through exhaled breath volatile organic compound analysis. *Medical Gas Research*. 2025; 15(2): 198-199. Available from: https://doi.org/10.4103/mgr.MEDGASRES-D-24-00101.

[15] Hao L, Huang G. An improved AdaBoost algorithm for identification of lung cancer based on electronic nose. *Heliyon*. 2023; 9(3): e13633. Available from: https://doi.org/10.1016/j.heliyon.2023.e13633.

[16] Binson VA, Mathew P, Thomas S, Mathew L. Detection of lung cancer and stages via breath analysis using a self-made electronic nose device. *Expert Review of Molecular Diagnostics*. 2024; 24(4): 341-353. Available from: https://doi.org/10.1080/14737159.2024.2316755.

[17] Binson VA, Subramoniam M, Mathew L. Discrimination of COPD and lung cancer from controls through breath analysis using a self-developed e-nose. *Journal of Breath Research*. 2021; 15(4): 046003. Available from: https://doi.org/10.1088/1752-7163/ac1326.

[18] Moshayedi AJ, Gharpure DC. Evaluation of bio inspired Mokhtar: Odor localization system. In: *2017 18th International Carpathian Control Conference (ICCC)*. Sinaia, Romania: IEEE; 2017. p.527-532. Available from: https://doi.org/10.1109/CarpathianCC.2017.7970457.

[19] Baglaeva I, Iaparov B, Zahradník I, Zahradníková A. Analysis of noisy transient signals based on Gaussian process regression. *Biophysical Journal*. 2023; 122(3): 451-459. Available from: https://doi.org/10.1016/j.bpj.2023.01.003.

[20] Geng K, Moshayedi JA, Chen J, Hu J, Zhang H. ENOSE performance in transient time and steady state area of gas sensor response for ammonia gas: Comparison and study. In: *Proceedings of the 2023 2nd Asia Conference on Algorithms, Computing and Machine Learning*. Shanghai, China: Asia Conference on Algorithms, Computing and Machine Learning; 2023. p.247-252. Available from: https://doi.org/10.1145/3590003.3590046.

[21] Ji H, Liu Y, Zhang R, Yuan Z, Meng F. Detection and recognition of toluene and butanone in mixture based on SnO_2 sensor via dynamic transient and steady-state response analysis in jump heating voltage mode. *Sensors and Actuators B: Chemical*. 2023; 376: 132969. Available from: https://doi.org/10.1016/j.snb.2022.132969.

[22] Naishadham K, Naishadham G, Cabrera N, Bekyarova E. Response surface modeling of the steady-state impedance responses of gas sensor arrays comprising functionalized carbon nanotubes to detect ozone and nitrogen dioxide. *Sensors*. 2023; 23(20): 8447. Available from: https://doi.org/10.3390/s23208447.

[23] Lee D, Jung J, Kim S, Kim H-D. Gas detection and recovery characteristics at room temperature observed in a Zr_3N_4-based memristor sensor array. *Sensors and Actuators B: Chemical*. 2023; 376: 132993. Available from: https://doi.org/10.1016/j.snb.2022.132993.

[24] Gutierrez-Osuna R, Nagle HT, Schiffman SS. Transient response analysis of an electronic nose using multi-exponential models. *Sensors and Actuators B: Chemical*. 1999; 61(1-3): 170-182. Available from: https://doi.org/10.1016/S0925-4005(99)00290-7.

[25] Hossein-Babaei F, Hosseini-Golgoo SM, Amini A. Extracting discriminative information from the Padé-Z-transformed responses of a temperature-modulated chemoresistive sensor for gas recognition. *Sensors and Actuators B: Chemical*. 2009; 142(1): 19-27. Available from: https://doi.org/10.1016/j.snb.2009.07.039.

[26] Seinfeld JH, Pandis SN. *Atmospheric Chemistry and Physics: From Air Pollution to Climate Change*. USA: John Wiley & Sons; 2016.

[27] Clifford PK, Tuma DT. Characteristics of semiconductor gas sensors I. Steady state gas response. *Sensors and Actuators*. 1982; 3: 233-254. Available from: https://doi.org/10.1016/0250-6874(82)80026-7.

[28] Wang W, Zhen Y, Zhang J, Li Y, Zhong H, Jia Z, et al. SnO_2 nanoparticles-modified 3D-multilayer MoS_2 nanosheets for ammonia gas sensing at room temperature. *Sensors and Actuators B: Chemical*. 2020; 321: 128471. Available from: https://doi.org/10.1016/j.snb.2020.128471.

[29] Acharyya S, Nag S, Kimbahune S, Ghose A, Pal A, Guha PK. Selective discrimination of VOCs applying gas sensing kinetic analysis over a metal oxide-based chemiresistive gas sensor. *ACS Sensors*. 2021; 6(6): 2218-2224. Available from: https://doi.org/10.1021/acssensors.1c00115.

[30] Monroy JG, González-Jiménez J, Blanco JL. Overcoming the slow recovery of MOX gas sensors through a system modeling approach. *Sensors*. 2012; 12(10): 13664-13680. Available from: https://doi.org/10.3390/s121013664.

[31] Moshayedi AJ, Khan AS, Chen M, Piccaluga PP. ENose: A new frontier for non-invasive cancer detection and monitoring. *Journal of Cancer Metastasis and Treatment*. 2025; 11: 6. Available from: https://doi.org/10.20517/2394-4722.2024.85.

[32] Varpula A, Novikov S, Haarahiltunen A, Kuivalainen P. Transient characterization techniques for resistive metal-oxide gas sensors. *Sensors and Actuators B: Chemical*. 2011; 159(1): 12-26. Available from: https://doi.org/10.1016/j.snb.2011.05.059.

[33] Mondal B, Meetei MS, Das J, Roy Chaudhuri C, Saha H. Quantitative recognition of flammable and toxic gases with artificial neural network using metal oxide gas sensors in embedded platform. *Engineering Science and Technology, an International Journal*. 2015; 18(2): 229-234. Available from: https://doi.org/10.1016/j.jestch.2014.12.010.

[34] Yesilata MY. *Machine learning based indoor air pollutant source recognition with gas resistance and multi-sensor array electronic noses*. Master's Thesis. Turkey: Middle East Technical University; 2022.

[35] Moshayedi AJ, Gharpure D. Implementing breath to improve response of gas sensors for leak detection in plume tracker robots. In: *Proceedings of the Third International Conference on Soft Computing for Problem Solving*. New Delhi, India: Springer; 2013. p.337-348. Available from: https://doi.org/10.1007/978-81-322-1768-8_31.

[36] Jang K-W, Choi J-H, Jeon J-H, Kim H-S. Combustible gas classification modeling using support vector machine and pairing plot scheme. *Sensors*. 2019; 19(22): 5018. Available from: https://doi.org/10.3390/s19225018.

[37] Binson VA, Subramoniam M, Sunny Y, Mathew L. Prediction of pulmonary diseases with electronic nose using SVM and XGBoost. *IEEE Sensors Journal*. 2021; 21(18): 20886-20895. Available from: https://doi.org/10.1109/JSEN.2021.3100390.

[38] Barea-Sepúlveda M, Ferreiro-González M, Calle JLP, Barbero GF, Ayuso J, Palma M. Comparison of different processing approaches by SVM and RF on HS-MS eNose and NIR Spectrometry data for the discrimination of gasoline samples. *Microchemical Journal*. 2022; 172: 106893. Available from: https://doi.org/10.1016/j.microc.2021.106893.

[39] Binson VA, Subramoniam M, Mathew L. Prediction of lung cancer with a sensor array based e-nose system using machine learning methods. *Microsystem Technologies*. 2024; 30: 1421-1434. Available from: https://doi.org/10.1007/s00542-024-05656-5.

[40] Gherman M-P, Cheng Y, Gomez A, Saukh O. Compensating altered sensitivity of duty-cycled MOX gas sensors with machine learning. In: *2021 18th Annual IEEE International Conference on Sensing, Communication, and*

Networking (SECON). Rome, Italy: IEEE; 2021. p.1-9. Available from: https://doi.org/10.1109/SECON52354.2021.9491586.

[41] Reimann P, Schütze A. Sensor arrays, virtual multisensors, data fusion, and gas sensor data evaluation. In: *Gas Sensing Fundamentals*. Heidelberg: Springer; 2014. p.67-107. Available from: https://doi.org/10.1007/5346_2013_52.

[42] Barsan N, Koziej D, Weimar U. Metal oxide-based gas sensor research: How to? *Sensors and Actuators B: Chemical*. 2007; 121(1): 18-35. Available from: https://doi.org/10.1016/j.snb.2006.09.047.

[43] Feng S, Farha F, Li Q, Wan Y, Xu Y, Zhang T, et al. Review on smart gas sensing technology. *Sensors*. 2019; 19(17): 3760. Available from: https://doi.org/10.3390/s19173760.

[44] Monroy JG, González-Jiménez J, Blanco JL. Overcoming the slow recovery of MOX gas sensors through a system modeling approach. *Sensors*. 2012; 12(10): 13664-13680. Available from: https://doi.org/10.3390/s121013664.

[45] Varpula A, Novikov S, Haarahiltunen A, Kuivalainen P. Transient characterization techniques for resistive metal-oxide gas sensors. *Sensors and Actuators B: Chemical*. 2011; 159(1): 12-26. Available from: https://doi.org/10.1016/j.snb.2011.05.059.

[46] Bikov A, Lázár Z, Horvath I. Established methodological issues in electronic nose research: How far are we from using these instruments in clinical settings of breath analysis? *Journal of Breath Research*. 2015; 9(3): 034001. Available from: https://doi.org/10.1088/1752-7155/9/3/034001.

[47] Ercolani C, Martinoli A. 3D odor source localization using a micro aerial vehicle: System design and performance evaluation. In: *2020 IEEE/RSJ International Conference on Intelligent Robots and Systems (IROS)*. Las Vegas, NV, USA: IEEE; 2020. p.6194-6200. Available from: https://doi.org/10.1109/IROS45743.2020.9341501.

[48] Zhang W, Wang L, Ye L, Li P, Hu M. Gas sensor array dynamic measurement uncertainty evaluation and optimization algorithm. *IEEE Access*. 2019; 7: 35779-35794. Available from: https://doi.org/10.1109/ACCESS.2019.2898881.

[49] Lin T, Lv X, Hu Z, Xu A, Feng C. Semiconductor metal oxides as chemoresistive sensors for detecting volatile organic compounds. *Sensors*. 2019; 19(2): 233. Available from: https://doi.org/10.3390/s19020233.

[50] Noori Skandari MH. Universal approximator property of the space of hyperbolic tangent functions. *Control and Optimization in Applied Mathematics*. 2018; 3(1): 75-85. Available from: https://doi.org/10.30473/coam.2019.45540.1111.

[51] Robin Y, Amann J, Schneider T, Schütze A, Bur C. Comparison of transfer learning and established calibration transfer methods for metal oxide semiconductor gas sensors. *Atmosphere*. 2023; 14(7): 1123. Available from: https://doi.org/10.3390/atmos14071123.

[52] Chen K, An R, Li C, Kang Y, Ma F, Zhao X, et al. Detection of ultra-low concentration acetylene gas dissolved in oil based on fiber-optic photoacoustic sensing. *Optics and Laser Technology*. 2022; 154: 108299. Available from: https://doi.org/10.1016/j.optlastec.2022.108299.

[53] Li Z, Yu J, Dong D, Yao G, Wei G, He A, et al. E-nose based on a high-integrated and low-power metal oxide gas sensor array. *Sensors and Actuators B: Chemical*. 2023; 380: 133289. Available from: https://doi.org/10.1016/j.snb.2023.133289.

[54] Zhang S, Zhang T. In situ detection of low amounts of ammonia. *Trends in Chemistry*. 2021; 3(5): 339-341. Available from: https://doi.org/10.1016/j.trechm.2021.03.001.

[55] Faul F, Erdfelder E, Lang A-G, Buchner A. G* power 3: A flexible statistical power analysis program for the social, behavioral, and biomedical sciences. *Behavior Research Methods*. 2007; 39(2): 175-191. Available from: https://doi.org/10.3758/BF03193146.

[56] Cohen J. *Statistical Power Analysis for the Behavioral Sciences*. USA: Routledge; 2013.

[57] Rudin W. *Principles of Mathematical Analysis*. 3rd ed. USA: McGraw-Hill; 1976.

Appendix: PPM calculation

Table 4. PPM formula the PPM formula calculations based on thanol volumes (0.1 mL to 1 mL), ethanol density (0.789 g/mL), and residence time are shown below. The residence time (min) is the time it takes for air to pass through the systemwith an inlet flow rate of 4 L/min

No	Calculation	Result/Description	Units
1	Volume calculations (V)	$\pi \times (2.5)^2 \times 15 = 294.52\ \text{cm}^3 = 0.2945\ \text{L}$	Volume of glass jar (cm^3 and L)
		$\pi \times (0.1)^2 \times 50 = 1.571\ \text{cm}^3 = 0.001571\ \text{L}$	Volume of pipe (cm^3 and L)
		$\pi \times (7.5)^2 \times 50 = 8839.256\ \text{cm}^3 = 8.839\ \text{L}$	Volume of main jar (cm^3 and L)
		9.132 L	Total volume (L)
2	Residence time (t)	$\frac{9.132}{4} = 2.283$ minutes	Time in minutes
3	Mass of ethanol (M)	Volume of ethanol (mL) × Density of ethanol (g/mL) × 1000 $(0.1 - 1) \times 0.789 \times 1000$	Mass in mg
4	Evaporation Rate (ER)	$\frac{\text{Mass of ethanol (mg)}}{10}$	Rate in mg/min
5	Concentration (ppm)	$\frac{\text{Mass of ethanol (mg)}}{4 \times 1000} \times 1000$	Concentration in ppm
6	Outlet flow rate (Q_{out})	Evaporation rate/ppm	Flow rate in L/min

Table 5. Parts per million (ppm), Ethanol volumes: 0.1 mL to 1 mL, TGS 2620 gas sensor ppm range: 50 ppm to 500 ppm. The total volume of the system is 9.132 L, which includes the volumes of Jar 1, Jar 2, and the connecting pipe. Inlet flow rate of 4 L/min, Outlet Flow Rate (Q_{out}), Inlet Flow Rate (Q_{in}), min: minutes. Ethanol Volume (EV), Mass of Ethanol (ME), Evaporation Rate (ER), Residence Time (RT)

PPM	EV (mL)	ME (mg)	ER (mg/min)	Q_{in} (L/min)	Q_{out} (L/min)	RT (min)
60	0.1	78.9	7.89	1.315	1.315	2.284
100	0.2	157.8	15.78	1.578	1.578	2.284
140	0.3	236.7	23.67	1.6907	1.6907	2.284
180	0.4	315.6	31.56	1.7533	1.7533	2.284
220	0.5	394.5	39.45	1.7932	1.7932	2.284
260	0.6	473.4	47.34	1.8208	1.8208	2.284
300	0.7	552.3	55.23	1.841	1.841	2.284
340	0.8	631.2	63.12	1.8565	1.8565	2.284
380	0.9	710.1	71.01	1.8687	1.8687	2.284
400	1.0	789.0	78.90	1.9725	1.9725	2.284